Article

Reliable Thermal-Physical Modeling of Lithium-Ion Batteries: Consistency between High-Frequency Impedance and Ion Transport

Gabriele Sordi [ID], Claudio Rabissi *[ID] and Andrea Casalegno

Department of Energy, Politecnico di Milano, Via Lambruschini 4, 20156 Milano, Italy;
gabriele.sordi@polimi.it (G.S.); andrea.casalegno@polimi.it (A.C.)
* Correspondence: claudio.rabissi@polimi.it

Abstract: Among lithium-ion battery diagnostic tests, electrochemical impedance spectroscopy, being highly informative on the physics of battery operation within limited testing times, deserves a prominent role in the identification of model parameters and the interpretation of battery state. Nevertheless, a reliable physical simulation and interpretation of battery impedance spectra is still to be addressed, due to its intrinsic complexity. An improved methodology for the calibration of a state-of-the-art physical model is hereby presented, focusing on high-energy batteries, which themselves require a careful focus on the high-frequency resistance of the impedance response. In this work, the common assumption of the infinite conductivity of the current collectors is questioned, presenting an improved methodology for simulating the pure resistance of the cell. This enables us to assign the proper contribution value to current collectors' resistance and, in turn, not to underestimate electrolyte conductivity, thereby preserving the physical relation between electrolyte conductivity and diffusivity and avoiding physical inconsistencies between impedance spectra and charge–discharge curves. The methodology is applied to the calibration of the model on a commercial sample, demonstrating the reliability and physical consistency of the solution with a set of discharge curves, EIS, and a dynamic driving cycle under a wide range of operating conditions.

Keywords: lithium-ion battery; EIS; parameter identification; modeling; electrolyte conductivity

1. Introduction

Lithium-ion battery (LIB) technology, featuring outstanding energy and power density, a satisfying lifetime, high round-trip efficiency, and very fast dynamics in a reasonably economic form [1,2], has rapidly become the undisputed ruler of portable power; it is now the main driver of the electrification in the transportation sector.

Despite the fully commercial development of the technology, researchers are still debating LIBs' degradation from a physical perspective, with the aid of reliable estimations of their state of health (SoH) and residual lifetime [3,4]. One relevant approach is the combined use of experiments and models.

In this regard, electrochemical impedance spectroscopy (EIS) [3,5–9] is a powerful non-invasive tool for lithium-ion battery characterization, providing a large amount of information discretized on a characteristic time scale and collected within a limited testing timespan. These advantages make it a promising tool for state-of-charge and state-of-health estimation [7,9]. However, EIS is difficult to interpret due to overlapping phenomena at similar frequencies, especially between the two electrodes. For instance, as explained in [5], in the medium frequency area, up to five phenomena can be present, whilst only some of them are easily detectable as an arc-shaped feature.

This complexity forces researchers to use models. EIS is usually modelled through equivalent circuit models (ECM) [3,6,7,10,11] of very miscellaneous complexity (within the literature), where relevant processes are associated with a combination of pure resistances

and capacitances whose values and layout are the design choice of the developer. In general, these models are very popular because of their simplicity, simulation velocity, and their potential compatibility with on-board vehicle applications for state-of-charge (SoC) or state-of-health estimation, as comprehensively explained in this recent review [12]. However, despite their advantages, ECMs do not include physical relations between elements; thus, they do not guarantee physical consistency in simulating battery operations. Moreover, they lack generalizability, as they are strongly sample-specific and condition-specific, providing poor performance if applied to broad operating conditions. Hence, their reliability has been questioned [13,14].

If time and computational effort are not the main drivers of model selection, physical models are more reliable. However, physical simulation of the impedance spectra of LIB is neither very common nor a simple task; it involves several tens of physical parameters that are often unknown or undeterminable. In previous publications [15,16], the authors analyzed the sensitivity of a number of physical parameters in an EIS simulated using the Doyle–Fuller–Newman (DFN) model, before proposing an optimized multi-measurement approach for model calibration, including guidelines for operating conditions' selection and model parameters' identification. These works identified that two key parameters in physical simulations are the electrolyte properties: ionic conductivity and lithium-ion diffusivity [16]. Their proper estimation is of paramount importance for a reliable simulation, together with their dependency on temperature and lithium concentration, enabling physically sound simulation of battery operations and interpretations of ageing. Despite these parameters being related via the known Nernst–Einstein relation [17], many models consider them independent parameters to ease the parameter identification process. However, this solution can lead to major physical inconsistencies, which arise from the wrong estimation of their contributions to the pure resistance of the device, here identified as high-frequency resistance (HFR); by this, we refer to the high-frequency intercept with the *x*-axis in the Nyquist plot of the EIS. On this topic, there is a gap between experiments, (from material to cell level) and models (from ECM to physical models). Indeed,

- many ECMs consider one pure resistor to account for all the ohmic losses, disregarding single contributions (for instance, electrodes' or current collectors' electric resistivities [3,6]. This choice lacks physical consistency and therefore limits simulation reliability.
- Moreover, these models usually consider the several elements independently of one other, potentially leading to physical inconsistencies, as in the case of electrolyte conductivity and diffusivity. According to the relevance of these two parameters for lithium-ion simulations, their relation [18] has to be ensured to provide a physically reliable simulation.

On the other hand, physical models

- usually reproduce discharge curves with satisfactory accuracy; however, to provide physical consistency when simulating LIB operation and dynamics, the reliability should be challenged using EIS, as recently pointed out by several research groups [16,17]. The simulation of EIS, and specifically of HFR, can guide the calibration by providing additional constraints to the solution.
- One interesting topic specific to HFR is the need to take into account the role of current collectors, which are often regarded as negligible [14,17]. Indeed, this choice can lead to wrong overestimation of electrolyte resistivity. In some conditions, the contribution of current collectors may be the major part of the pure response of the device, especially in high-energy designs; thus, the assumption of infinite conductivity applied in many models such as DFN is not valid.

To summarize, to the authors knowledge, no work in the literature debates the actual contribution of the electrolyte in the HFR of lithium-ion batteries from a physical perspective. Hence, in this work, starting from the analysis of one experimental high-energy case study and providing guidelines for a general approach, we discuss the reliable simulation of the battery's ohmic resistance, proposing an improved modeling framework and imple-

menting the findings in an optimized parameter identification procedure for a DFN model, which demonstrates its improved reliability.

The outline of this research paper is as follows. Section 2 summarizes the fundamentals of the DFN physical model and the description of experimental setup and tested battery samples. In Section 3, the cells are dismantled and the current collectors' resistance is directly measured. Moreover, a discussion on the magnitude of the electrolyte and current collectors' resistance is presented. Lastly, Section 4 reports the optimized parameter identification procedure, together with the results and a wide validation against different experimental curves, from full discharges to EIS, in different operating conditions.

2. Methodology

2.1. Battery Samples

One type of high-energy commercial cell is adopted in this work. Its specifications are listed in Table 1.

Table 1. Specifications of experimental samples.

Model	SONY US18650V3
Geometry	Cylindrical 18650
Anode chemistry	Graphite
Cathode chemistry	NMC
Nominal capacity	2250 mAh
Maximum current (C-rate)	Charge: 2.25 A (1C) Discharge: 10 A (4.5C)
Operative voltage range	4.2 V–2.5 V
Temperature range charge/discharge	Charge: 0–45 °C Discharge: −20 °C/60 °C
Weight	44 g

The electrolyte is expected to be a mixture of $LiPF_6$ in EC:DMC solvent.

Measurements of the internal geometry were performed after dismantling two samples that were completely discharged to 0 V and short-circuited, for the sake of process safety. Images of the battery dismantling process are given in Figure 1, together with a simplified scheme of the internal structure, while the geometrical dimensions of all the components are listed in Table 2. The cell active area is computed as the frontal surface of the smaller active layer, which is the positive electrode.
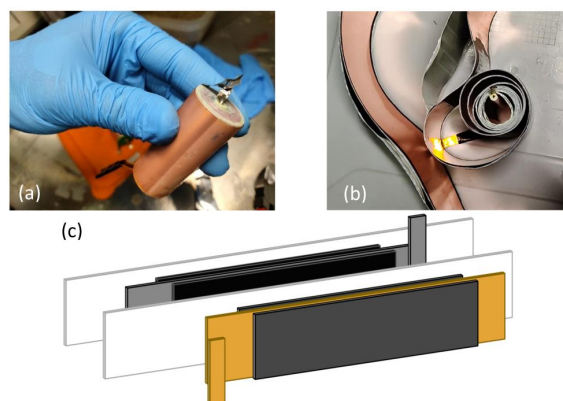
Figure 1. Views of the opened sample: (**a**) after case removal, with jelly roll still winded; (**b**) during the unwinding of the jelly roll. (**c**) Simplified scheme of current collectors and tabs of both the electrodes. Colors: copper foil in orange, aluminum foil in grey, separator in white, and active materials in black, respectively.

Table 2. Internal dimensions of battery layers.

US18650V3					
	Component	Layers	L (cm)	H (cm)	W (μm)
Negative	Current collector (Copper)	1	66.5	5.7	15
	Active layer (Graphite)	2	58.5	5.7	70
Positive	Current collector (Aluminum)	1	65.8	5.7	20
	Active layer (NMC)	2	56.5	5.7	65
	Separator	2	80.3	5.7	15
	Active area (cm^2)			644.10	

As is visible in the scheme, battery the jelly roll is composed of copper and aluminum current collectors, respectively, covered on both sides with negative (graphite) and positive (NMC) electrode layers. Beneath such active layers, the separator is winded in a twofold configuration, creating a two-layer battery roll as the elementary unit.

2.2. Experimental Testbench

The experimental testbench is a custom-developed testing station constituted by a NI-4124 power supply (current uncertainty: $\pm 0.5\% \pm 0.1\%$ FSR) and two modular Chroma UM 63640-80-80 electronic loads (voltage/current uncertainty: $\pm 0.025\% \pm 0.01\%$ FSR/$\pm 0.1\% \pm 0.1\%$ FSR), resulting in a cycler of eight independent channels with impedance measurement capability. This setup is employed in all the measurements required for model parameter identification and reliability validation. Details on the testbench are provided in publication [16].

For measurement of the current collectors' resistance, an Autolab PGSTAT30 potentiostat/galvanostat equipped with a frequency response analyser board (FRA2) is used. Both resistance measurement and impedance measurement are conducted during a pulse, providing very similar results.

2.3. Physical Model

The simulations are performed using a classical DFN model implemented in COMSOL Multiphysics®. The model includes double-layer (dis/)charging on the surface of both electrodes, and surficial passive layers are modeled as lumped resistances. The model is coupled with a 2D thermal model to account for heat generation inside the cell, and many parameters are temperature-dependent, such as kinetic constants and diffusivities. The electrochemical model computes the heat generation, so that the thermal model computes the temperature distribution over the cross section of a cylindrical cell. In turn, the thermal model provides an average temperature to update the temperature-dependent parameter values.

For a detailed description of the equations of the DFN and thermal model, we refer the reader to [15,16]. EIS is simulated in the time domain and then converted into a frequency domain by way of fast Fourier transform, as discussed in [15,16]. Optimization of EIS simulation has been performed as detailed in Section 4.2.

3. Focus on Cell High-Frequency Resistance

3.1. High-Frequency Resistance at Different SoC and Temperatures

Figure 2a reports experimental HFR values measured at different temperatures and states of charge, expressed both as total and specific resistance with respect to battery internal surface. Figure 2b shows the corresponding frequency, obtained through interpolation of experimental data at a null imaginary component of the impedance. A weak dependance on the state of charge is detected for all the temperatures, where HFR is 2–3 mΩ larger at low SOC than high SoC. Temperature affects the HFR value, but in the investigated interval, its effect appears as a minor contribution (within 10%). Differently, frequency is

strongly affected by temperature, and diminishes significantly as the temperature increases, as expected.
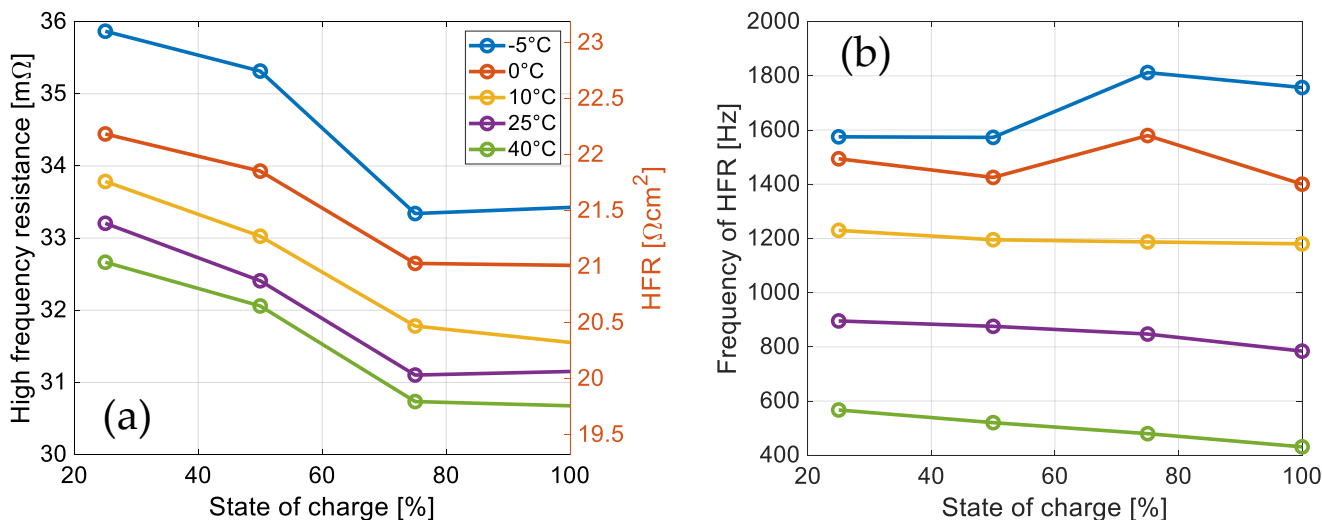
Figure 2. Value of (**a**) the high-frequency resistance and (**b**) its frequency as a function of cell temperature and state of charge.

Being a purely resistive feature of overall battery impedance response, its known contributing terms are identifiable in electrolyte ionic resistance, the electric resistance of current collectors (usually neglected under the assumption of infinite conductivity), and external resistance (comprising the electrical and contact resistances of the external circuit). In the following, the first two contributions are investigated.

3.2. Electrolyte Ionic Resistance

In the literature, $LiPF_6$ electrolyte ionic conductivity has been extensively characterized [19]. Figure 3 reports the trends of the ionic conductivity with the temperature and concentration of a mixture of PC-EC-DMC with $LiPF_6$, by exploiting the empirical correlation proposed in [19] that was validated over experimental data.
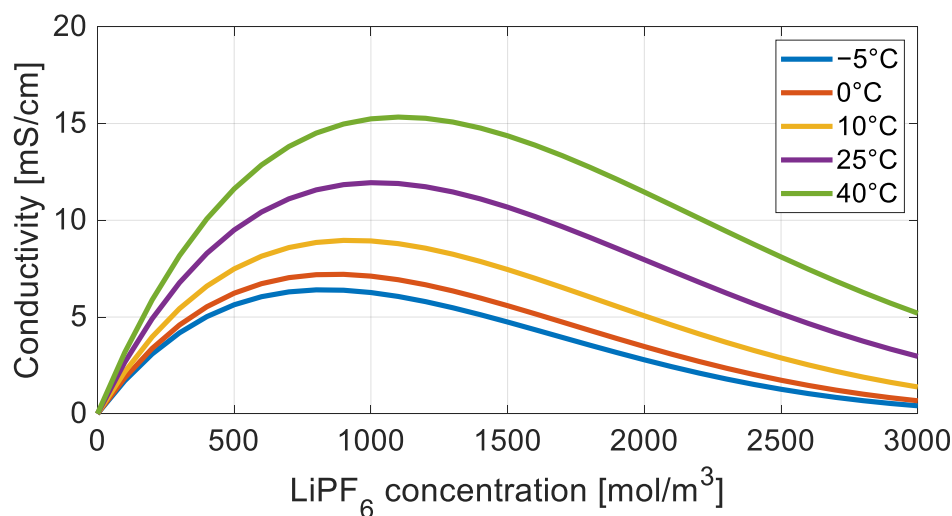
Figure 3. Electrolyte conductivity as a function of lithium concentration and temperature for a mixture of PC-EC-DMC with $LiPF_6$. From the curves are obtained through the empirical correlation proposed in [19]. Temperatures are selected to ease the comparison with Figure 2.

For the purpose of this publication, such electrolyte conductivity dependance on lithium concentration and temperature is accounted for as follows [19]:

$$\sigma_e = cond_{el} \cdot c_e \cdot \left(-10.5 + 0.0740 \cdot T - 6.96 \times 10^{-5} \cdot T^2 + 0.668 \cdot c_e - 0.0178 c_e \cdot T + 2.8 \times 10^{-5} \cdot c_e \cdot T^2 + 0.494 \cdot c_e^2 - 8.86 \times 10^{-4} \cdot c_e^2 \cdot T \right)^2 \quad (1)$$

where c_e $[\mathrm{mol/m^3}]$ is the lithium concentration in the electrolyte, T [K] is the temperature, and $cond_{el}$ is a coefficient dependent on the specific sample. This solution maintains a physically sound relation with operating conditions while adopting a fitting parameter, the exact electrolyte composition being unknown. As is clear from the figure and the correlation, the peak value at 40 °C is 50% larger than the corresponding value at 20 °C, showing a sensible temperature dependency. Similarly, the conductivity decreases significantly, being far from the optimized lithium concentration (around 1000–1200 mol/m^3).

To roughly quantify the electrolyte contribution to the overall cell-specific HFR, electrolyte specific resistance can be calculated, considering the standard electrolyte conductivity at 25 °C [19] (see Figure 3) and cell internal geometry discussed in Section 2.1. For the samples under investigation, the specific electrolyte ionic resistance is estimated between 2.5–3.5 $\Omega \cdot \mathrm{cm^2}$ (depending on the separator and electrode porosity, considered to consistently between 40 and 50% of the high-energy battery typology); this range covers just a small portion of the total HFR (measured in 20–21 $\Omega \cdot \mathrm{cm^2}$, depending on battery SOC at 25 °C, as reported in Figure 2a). Additionally, as is clear from Figure 3, the variation in electrolyte conductivity with temperature is sensible (~+30% if temperature is increased from 20 °C to 40 °C, and ~−30% from 20 °C to −10 °C), while HFR variation is clearly narrower. Therefore, it is implicit that the electrolyte is not always the only nor the main element responsible for the HFR value.

Moreover, physical consistency should be discussed. Indeed, both the lithium diffusion coefficient and ionic conductivity are related through the Nernst–Einstein equation [17]:

$$D_e = \sigma_e \cdot \frac{RT}{F^2 c_e} \quad (2)$$

where D_e and σ_e are the diffusion coefficient and electrolyte conductivity in $[\mathrm{m^2/s}]$ and [S/m], respectively, $R = 8.314\,\mathrm{J/(mol \cdot K)}$ is the gas constant, T is the temperature in [K], $F = 96,485\,\mathrm{C/mol}$ Faraday constant, and c_e is the lithium concentration in the electrolyte in $[\mathrm{mol/m^3}]$.

Associating the HFR value of the electrolyte would only lead to additional major mistakes affecting the electrolyte diffusivity, thereby depleting the reliability and physical soundness of the model.

3.3. Current Collectors' Electrical Resistance

To aid the discussion of current collectors' contribution to HFR, whose value is hardly present in physical models (according to the common assumption of infinite conductivity), a simplified scheme is provided in Figure 4.

Current collectors can be approximated with thin foils with one tab each. Tabs connect the aluminum and copper foils with the corresponding poles of the battery, and can be considered lumped resistances; their position and number significantly affect the current distribution within current collectors. Indeed, if each foil is connected to a single tab, the overall current will flow through it; however, in the case of more tabs per foil, the overall current is split between them, and their ohmic contribution will be lower.

Moreover, if the tab is placed at the edge of the foils, as in Figure 4, the overall current will have to reach the tab; under the assumption of uniform reaction rate, the current will be maximum at the tab position, and will linearly decrease to zero at the opposite edge. Hence, the average current is half of the overall value. Instead, if the tab is placed at the middle of the foil, the current will have to flow through only half of the overall foil length, making the average current one fourth of the total value. Hence, generally, the more tabs per pole are present, and the better distributed they are, the lower the effective current collector resistance becomes.
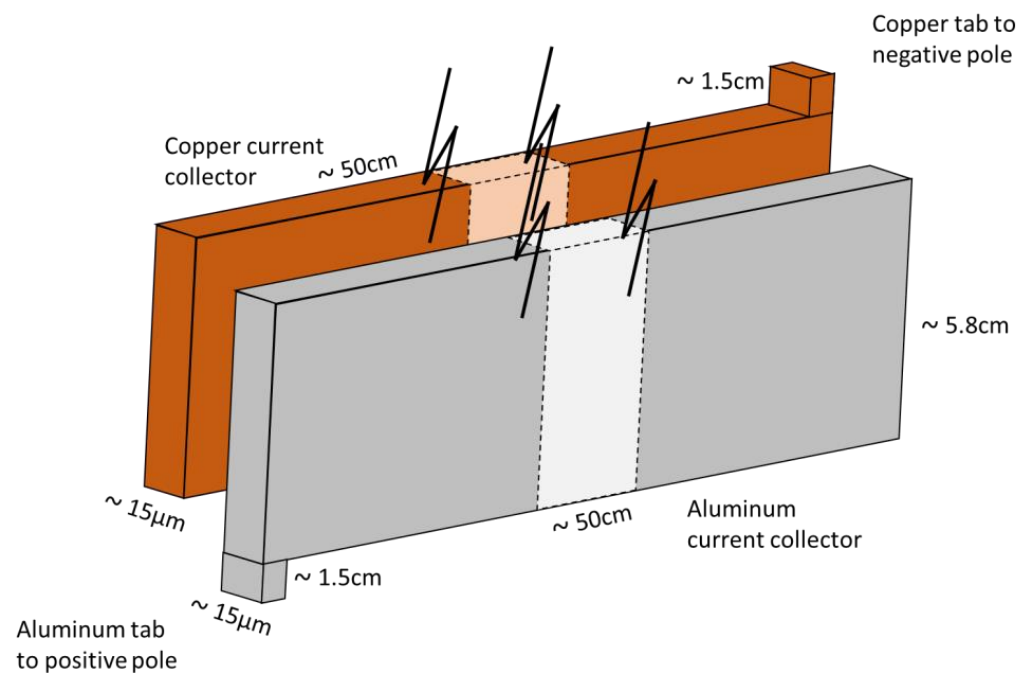
Figure 4. Simplified scheme of current collectors.

In order to take into account the lumped resistance part of the internal circuit of the battery, namely caps, tabs and their soldering, which have a non-trivial value, the overall resistance is experimentally measured, and the resulting values are reported in Table 3. The resistance is measured through a current pulse along the roll, with and without both tab and cap. The current collectors' contribution is halved according to the assumption of uniform current generation along the foils.

Table 3. Current collectors' resistance measurement.

Current Collector Material	Tab Number and Position	Half CC Only		Overall (Full CC, Tabs and Cap)	
		Total [mΩ]	Specific [Ωcm^2]	Total [mΩ]	Specific [Ωcm^2]
Copper	1, outer edge	11.5	7407	28	18,035
Aluminum	1, inner edge	11.3	7278	24	15,458

From this measurement, the current collectors proved to cover a relevant portion of the HFR, deserving to be included in the model. It is worth to remind that this is specific to the case of high-energy batteries, and may change significantly in the case of a different cell design, which is outside the scope of this publication.

3.4. Modelling the Current Collectors' Resistance

The physical model requires a proper implementation of current collectors' role for a consistent simulation of the related phenomenon. Hence, a dedicated internal resistance term, R_{int}, is introduced in the model to embed the current collectors' resistance. The cell voltage ΔV is now computed as follows:

$$\Delta V = \varphi_s|_{x=L_n+L_{sep}+L_p} - \varphi_s|_{x=0} - R_{int}I \tag{3}$$

where $\varphi_s|_{x=L_n+L_{sep}+L_p}$ and $\varphi_s|_{x=0}$ are the electric potential as the electrode–current collector interface of the positive and negative electrodes, respectively, while R_{int} and I are the internal resistance and total applied current, respectively.

Correspondingly, the heat generation term is modified to include a heat generation due to the Joule effect, itself due to the internal resistance term, which can severely affect battery operation, especially during high-current operation:

$$\frac{1}{r}\frac{\partial}{\partial r}\left(r\,k_T\frac{\partial T}{\partial r}\right) + \frac{\partial}{\partial z}\left(k_T\frac{\partial T}{\partial z}\right) + \overline{q_{gen}} + R_{int}\,I^2 = \rho C\frac{\partial T}{\partial t} \tag{4}$$

where r is the radial coordinate in the cylindrical cell, k_T the average thermal conductivity of active area of the cell, z the vertical height coordinate, T the cell temperature, $\overline{q_{gen}}$ the heat generation obtained in the P2D model, ρ the cell density and C the cell heat capacity.

As described in Section 3.2, the current collector resistance depends on different design aspects, such as the length and number and position of tabs. It is not possible to state a general rule for its estimation without prior knowledge of the battery geometry. In the following, the parameter R_{int} is considered a fitting parameter. However, since its contribution is known to be a pure resistance, a correlation with the HFR value is proposed to constrain the parameter identification problem, as will be discussed in Section 4.2:

$$R_{int} = HFR_{exp} - R_0 - R_{el} \tag{5}$$

$$R_{el} = \frac{K_1}{\sigma_{el}} \tag{6}$$

where HFR_{exp} is the HFR value measured at 25 °C, 50% SoC. It is assumed that it is equal to the sum of three terms: the electrolyte contribution R_{el}, computed as the ratio between a constant K_1 and the conductivity, the internal resistance, and R_0, which is the sum of all the other resistive terms of the battery, such as the electronic conductivities of the electrodes. In practice, R_0 is the modeled cell impedance at the same operating conditions, but with the electrolyte conductivity σ_{el} equal to 1000 S/m and R_{int} equal to zero; thus, the contributions of electrolyte and internal resistance are negligible. In the present case, the constants R_0 and K_1 are equal to 2.3 mΩ and 1.39 1/m, respectively.

4. Results and Discussion

4.1. Diagnostic Protocol

A previously performed sensitivity analysis [16] upon discharge test, EIS and relaxation test demonstrated that low temperature and extreme SOC conditions can maximise the experimental identifiability of the model parameters.

Summarizing the main points:

- Measuring EIS spectra is of great importance, at least at two opposite states of charge, to enable a distinction between positive and negative electrode contributions, and at two temperature levels, to enable the calibration of temperature-related parameters.
- The discharge test is mainly sensitive to diffusion-related phenomena, both in electrodes' bulk and the electrolyte. Two combinations of C-rates and temperatures are advised to be covered with this technique, spanning the entire battery capacity.

Applying the methodology to the sample, the resulting experimental protocol is reported in Figure 5:

- (E1) EIS testing on the battery at SoC 100%, 10 °C is performed at 20 logarithmically spaced frequencies in the range 4000–1 Hz;
- (D1) the battery is discharged at 2C with a DoD 50%;
- (R) a relaxation test of 1000 s follows the discharge. During this test, voltage and temperature are recorded;
- (E2) after the relaxation, the climate chamber temperature of 25 °C is set, and when the temperature is reached, an EIS at SoC 50% within the same frequency interval as the first is performed;

- (D2) the battery is discharged at 1C until the lower voltage limit is reached (theoretical DoD 50%).
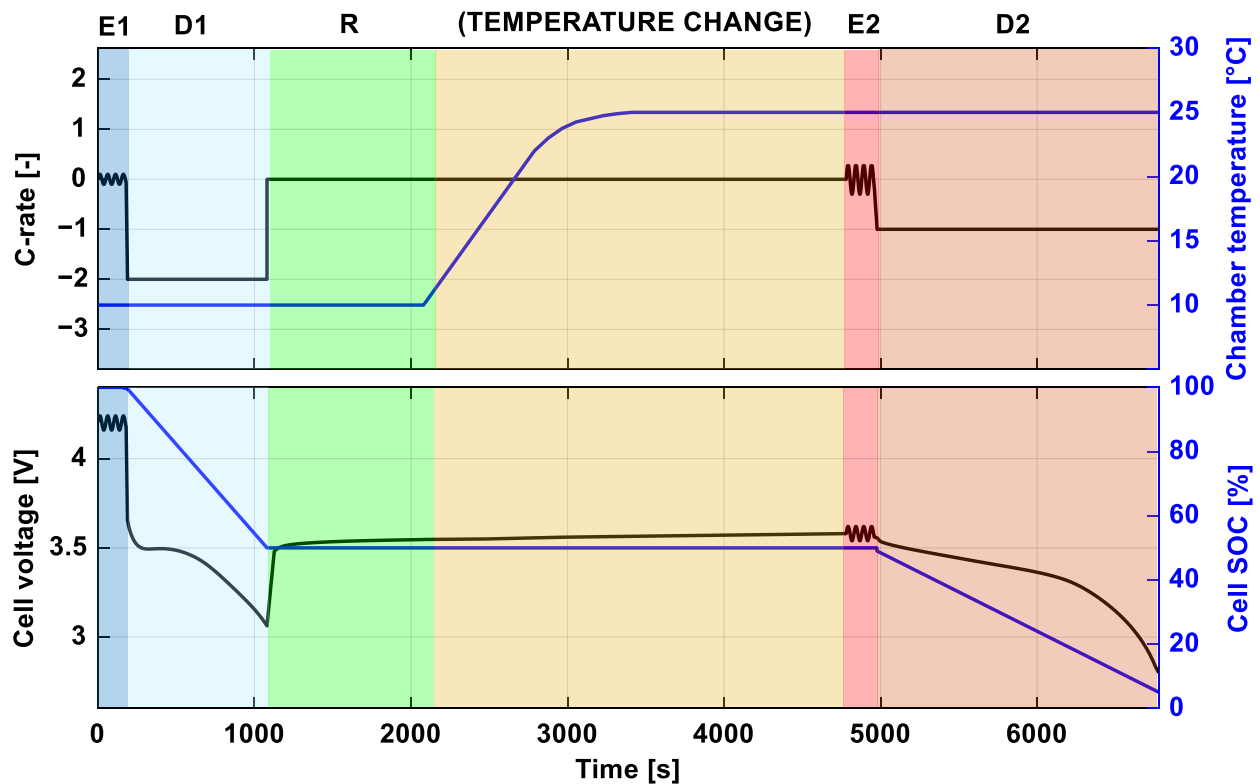
Figure 5. Depiction of the proposed protocol, reporting control variables in the upper panel (black: C-rate and blue: temperature) and resulting variables in the lower panel (black: cell voltage and blue: SOC) over time. Background colors indicate each different diagnostic techniques (dark blue: E1, light blue: D1, green: R, yellow: temperature change, red: E2, orange: D2) as detailed in the text.

4.2. Optimized EIS Simulation and Parameter Identification Procedure

After the implementation of the internal resistance term in the battery model (as described in previous section), an optimized stepwise calibration procedure is developed. Optimizations in the EIS simulation to improve the convergence time and reliability are also implemented, as described in the following:

- **Optimized domain**

Because lithium diffusion in electrodes' bulk is a slow phenomenon, its effect does not impact the performance until the imposed sine frequency approaches low values. Hence, spatial gradients in the particles were neglected during the high-frequency part of the EIS ($f \geq 10$ Hz), imposing the equality of lithium concentration between surface and canter of the particles, solving Fick's law for diffusion only at ($f \leq 10$ Hz). The exact frequency threshold is case-dependent; therefore, a conservative approach should be applied to un-bias the solution. 10 Hz is selected in this specific case.

- **Optimized mesh resolution**

An optimization of mesh resolution of the electrochemical model is introduced. A highly resolved mesh is crucial for the simulation of highly heterogeneous conditions such as those originating during discharges, especially at a high C-rate; it is less important during EIS simulations performed at a low C-rate in open-circuit conditions (OCV) under a steady-state assumption. Hence, it is reduced in the order of 5 points per domain along the x direction (electrode thickness), without losing accuracy, during EIS simulation.

- **Optimized thermal model**

  In an EIS measurement, the applied sinusoidal current is very low, and the heat generated by the cell in this condition can be reasonably neglected. Hence, in an EIS study, the heath transfer computation is deactivated, while it is maintained for the discharges.

Stepwise Single-Measurement Calibration

An optimized stepwise approach is developed and implemented, exploiting the separation between the experimental techniques and corresponding physical parameters demonstrated in the sensitivity analysis [16]. Therefore, the parameter identification problem is solved with a three-step procedure:

- Step 1: the model is calibrated against the two impedance spectra (E1) and (E2) simultaneously, by optimizing the **kinetic constants** (k_{pos}, k_{neg}) and **double-layer capacitances** values ($C_{dl,pos}$, $C_{dl,neg}$). In this step, only the charge transfer resistance is considered; hence, the HFR value is neglected, and the remaining parameters are fixed at a proper literature value, as listed in Table 4. The other parameters are fixed to an intermediate value within the literature's range, as a first guess. Since solid diffusivities and (to a certain extent) electrolyte properties have a minor effect on EIS, this solution is viable and will be corroborated Step 3. At this stage, the current collectors' contribution is estimated according to Equation (5), presented in Section 3.4, corresponding to an intermediate value of electrolyte conductivity from the literature.
- Step 2: the model is then calibrated on partial discharges (D1) and (D2) by optimizing the **solid diffusivities** ($D_{s,pos}$, $D_{s,neg}$) and **electrolyte conductivity** ($cond_{el}$).
- Step 3: finally, Step 1 is repeated, employing the solid diffusivities and electrolyte conductivity computed in Step 2.

Table 4. List of main physical parameters with the corresponding literature range and selected value for the case study. The interval of $cond_{el}$ variation was estimated so that the conductivity of the electrolyte falls within the range identified in the references.

Parameters	Symbol	Variability Interval Employed in This Work	References
Kinetic rate constant of the cathode	k_{pos} [m/s]	$[2.5 \times 10^{-11}; 1 \times 10^{-8}]$	[20,21]
Kinetic rate constant of the anode	k_{neg} [m/s]	$[2.5 \times 10^{-11}; 1 \times 10^{-8}]$	[20,21]
Double layer of the cathode	$C_{dl,pos}$ [F/m^2]	$[0.05; 25]$	[22,23]
Double layer of the anode	$C_{dl,neg}$ [F/m^2]	$[0.05; 25]$	[22,23]
Ionic conductivity factor	$cond_{el}$ [−]	$[0.05; 1.25]$	[19,24]
Solid diffusivity of the cathode	$D_{s,pos}$ [m^2/s]	$[1 \times 10^{-6}; 1 \times 10^{-12}]$	[18,25,26]
Solid diffusivity of the anode	$D_{s,neg}$ [m^2/s]	$[5 \times 10^{-6}; 5 \times 10^{-12}]$	[18,27]

4.3. Obtained Solution

The calibration is performed twice to check its repeatability; the result is presented in Table 5, while the experimental and simulated measurements involved in the protocol are shown in Figure 6.

Table 5. Values of the parameters obtained with the step calibration procedure.

Parameter	Value
$k_{pos}\ [\text{m/s}]$	8.44×10^{-9}
$k_{neg}\ [\text{m/s}]$	9.92×10^{-10}
$cond_{el}\ [-]$	0.475
$C_{dl,pos}\ [\text{F/m}^2]$	0.341
$C_{dl,neg}\ [\text{F/m}^2]$	0.267
$D_{s,pos}\ [\text{m}^{2/}\text{s}]$	9.87×10^{-14}
$D_{s,neg}\ [\text{m}^2/\text{s}]$	1.24×10^{-14}
$R_{int}\ [\Omega]$	2.63×10^{-2}
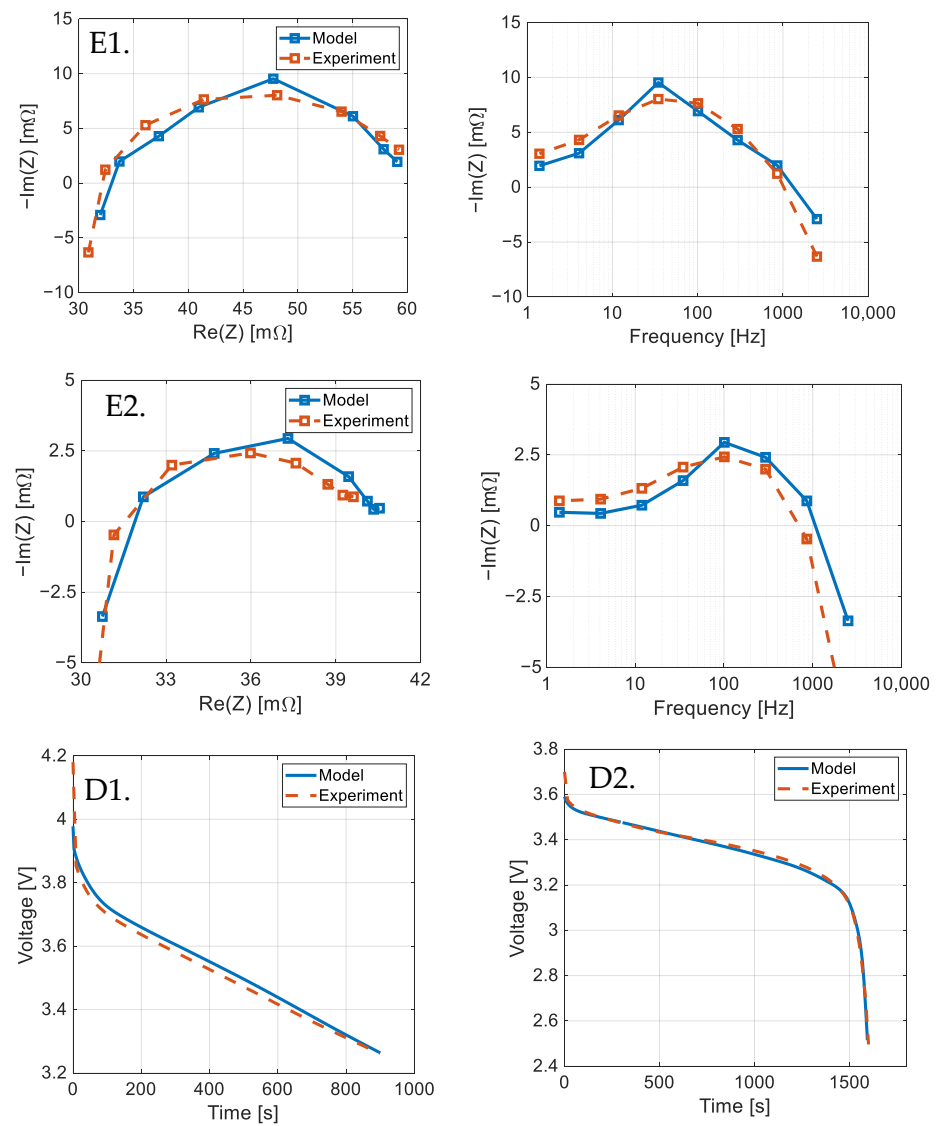
Figure 6. Comparison between experimental (dashed orange lines) curves of the diagnostic protocol and the corresponding modelled ones (full blue). **E1**—Impedance spectrum and Bode plot of the imaginary component at 10 °C, SoC 100%; **E2**–Impedance spectrum and Bode plot of the imaginary component at 25 °C, SoC 50%; **D1**–Discharge curve at 2C, 10 °C, from 100% SoC to 50% SoC and **D2**—at 1C, 25 °C, from 50% SoC to 0% SoC.

4.4. Validation

To validate the obtained results, a set of non-training conditions and operation modes were simulated with the calibrated model, and compared with experimental measurements. The validation dataset includes (as listed in Table 6)

Table 6. List of measurements belonging to the validation dataset and corresponding RMSE values, obtained through Equation (7), by comparing modelled and experimental curves. For discharge curves, the RMSEs computed over the full discharge (left value) and from SoC 100% to 3 V (right value) are provided.

| Technique	Operating Condition	RMSE
	$0.5C, 45\,^\circ C, 100\% - 0\%\,SoC$	$60.3\,\text{mV}; 23.6\,\text{mV}$
	$1C, 10\,^\circ C, 100\% - 0\%\,SoC$	$66.2\,\text{mV}; 34.9\,\text{mV}$
Discharge curve	$1C, 25\,^\circ C, 100\% - 0\%\,SoC$	$25.9\,\text{mV}; 18.3\,\text{mV}$
	$1C, 45\,^\circ C, 100\% - 0\%\,SoC$	$14.5\,\text{mV}; 11.5\,\text{mV}$
	$2C, 25\,^\circ C, 100\% - 0\%\,SoC$	$44.4\,\text{mV}; 18.6\,\text{mV}$
	$2C, 45\,^\circ C, 100\% - 0\%\,SoC$	$50.9\,\text{mV}; 29.2\,\text{mV}$
	$45\,^\circ C, 100\%\,SoC$	$Z_{Re} : 0.9\,\text{m}\Omega$
		$Z_{Im} : 2.0\,\text{m}\Omega$
	$10\,^\circ C, 75\%\,SoC$	$Z_{Re} : 4.0\,\text{m}\Omega$
		$Z_{Im} : 3.3\,\text{m}\Omega$
EIS	$25\,^\circ C, 75\%\,SoC$	$Z_{Re} : 1.8\,\text{m}\Omega$
		$Z_{Im} : 2.4\,\text{m}\Omega$
	$45\,^\circ C, 75\%\,SoC$	$Z_{Re} : 1.3\,\text{m}\Omega$
		$Z_{Im} : 2.2\,\text{m}\Omega$
IEC 62660-1:2018	$25\,^\circ C, 100\% - 0\%\,SoC$	$5.6\,\text{mV}$

- Full discharges at
    - 0.5C at 45 °C
    - 1C, 10–25–45 °C
    - 2C, 25–45 °C
- EIS spectra performed from 4 kHz to 20 mHz, with 40 logarithmically spaced points:
    - At SoC 75% and 10–25–45 °C
    - At 100% SoC and 45 °C;
- The application of the IEC 62660-1:2018 BEV cycle life profile [28], as a highly dynamic profile, at 25 °C, from SoC 100% to the lower voltage threshold.

To quantify the average distance between the experimental and the model curves, the point-by-point root mean square error (*RMSE*) is computed as:

$$RMSE = \sqrt{\frac{\sum_{i=1}^{N} \left(x_i^e - x_i^m \right)^2}{N}} \tag{7}$$

where x_i^e is the experimental data, x_i^m the simulated data, and N the number of sampled points.

*RMSE*s are reported in Table 6, while experimental and simulated profiles are shown in Figure 7.
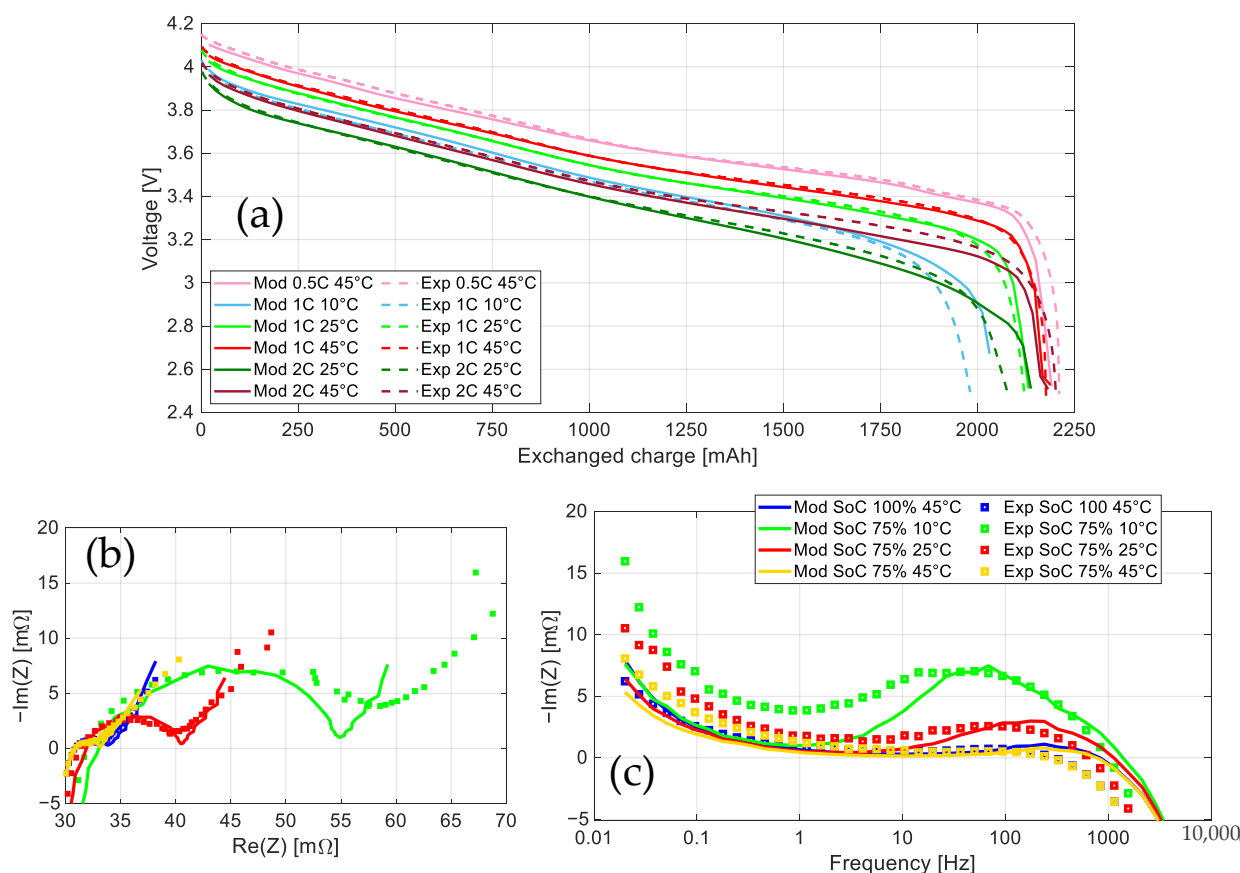
Figure 7. Comparison under various conditions (described in the legends) between (**a**) the experimental (dashed lines) discharges belonging to the validation dataset and the corresponding modelled ones (full lines), and the Nyquist (**b**) and Bode (**c**) plots of the experimental (squared markers) EIS of the validation dataset, and the corresponding modelled EIS (full lines).

In the latter, the model simulations are satisfactory for large portions of the discharge in all the operating conditions. This result proves the reliability of the model in reproducing the losses at different temperatures and C-rates. From a quantitative point of view, by comparing the RMSE listed in Table 6 with literature values, these values are slightly higher than the average. Indeed, Park et al. [29], worked with a nickel–cobalt–aluminum oxide cell battery and reported RMSEs of 25.5 mV and 11.8 mV, respectively, for a 1C and 0.5C discharge, both at 25 °C. Li et al. [30] calibrated a $LiMnO_4/LiC_6$ battery and obtained RMSEs between 6.4 mV and 12.9 mV for discharges at room temperature, with C-rates in the range 0.5C–3C. The highest average error was achieved in the 0.5C discharge. Lastly, Yang et al. [31] utilized NMC cells and obtained RMSEs of 15.6 mV, 14.6 mV and 21.6 mV, for discharges at 25 °C and C-rates 1C, 1.5C and 2C, respectively. However, all the works focused on a limited range of operating conditions, which can justify lower RMSEs values. The current results suffer from high errors at the end of discharge, where, due to the steep OCP curve of graphite, little misalignments lead to a sensible effect on the estimated voltage. To highlight this consideration, RMSEs were also evaluated from fully charged conditions down to 3 V (right values in Table 6). Overall, the results proved to be largely satisfactory for almost all the combinations of temperature, C-rate, and SoC analyzed herein.

With regards to Figure 7b,c, the EIS spectrum is reasonably reproduced in all the cases. The magnitude of the kinetic loop matches at all the temperatures; thus, the kinetic variation with temperature is reliably implemented in the model. Similarly, the HFR value reasonably varies with temperature, demonstrating the proper implementation of resistive

features. The diffusive branch at low frequency is also reasonably reproduced thanks to the proper identification of diffusive properties in the discharges of the protocol. From the Bode plot, the characteristic frequencies of the model are in line with those of the experiments. From a quantitative point of view, the simulation of EIS using a physical model is seldom performed in the literature. Overall, the RMSEs values are considered satisfactory for the purposes of the work.

Lastly, with reference to Figure 8, the model reliability is further corroborated with the simulation of a dynamic profile. The very low RMSE value proves the proper simulation of overpotentials and the internal state of the battery over the vast majority of the state-of-charge window.
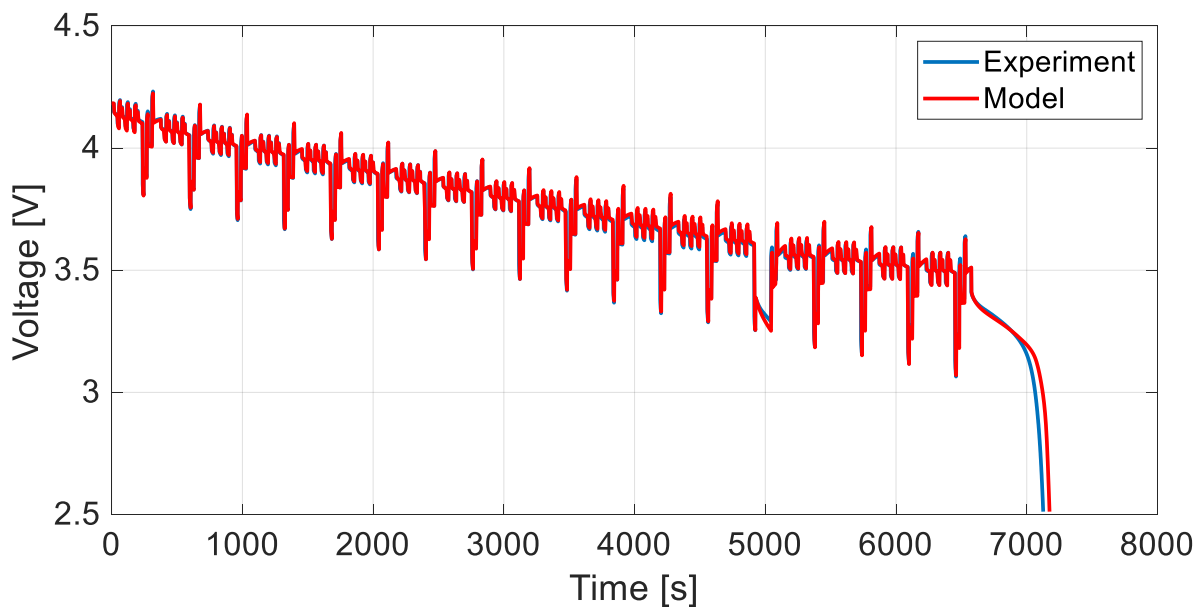
Figure 8. Comparison between the experimental IEC 62660-1:2018 BEV cycle profile belonging to the validation dataset and the corresponding modelled one.

5. Conclusions

This work discussed the proper implementation of an internal circuit contribution to lithium-ion batteries' impedance for a reliable and physically sound simulation of the role of the electrolyte. Indeed, considering typical electrolyte conductivity values as a function of temperature, and measuring the resistance of current collectors, it was shown that the latter covers a non-negligible portion of the high-frequency resistance (HFR) of the battery, which also features an apparently inconsistent trend with temperature. A proper modeling of this effect is proposed, accounting for ohmic loss and the Joule effect, to prevent the underestimation of the electrolyte conductivity (which may lead to physical inconsistencies, thereby negating the relationship between electrolyte conductivity and diffusivity).

The proposed methodology is applied to identify the model parameter values of one commercial sample, exploiting a compact multi-measurement experimental protocol together with an optimized stepwise procedure. The resulting set of parameter values reproduce the experimental curves suitably. Moreover, the physical consistency of the obtained solution is demonstrated against a wide validation dataset in terms of operating conditions. The results were compared to similar works in the literature, demonstrating slightly higher RMSE values, but over a much broader range of operating conditions, including EIS simulation. Moreover, the model shows the capability of assigning the phenomena to the proper characteristic time, and simulating temperature variations properly. Therefore, all in all, the results are considered consistently satisfactory, first overcoming initial limitations and, in turn, showing the reliability of the proposed methodology.

List of Acronyms

Acronym	Description
CC	Constant current
D1	First discharge of the developed diagnostic protocol
D2	Second discharge of the developed diagnostic protocol
DFN	Doyle–Fuller–Newman physical model
DOD	Depth of discharge
E1	First EIS of the developed diagnostic protocol
E2	Second EIS of the developed diagnostic protocol
ECM	Equivalent circuit model
EIS	Electrochemical impedance spectroscopy
FFT	Fast Fourier transform
FR	Fast relaxation time
GITT	Galvanostatic intermittent titration technique
HF	High frequency
HFR	High-frequency resistance
LF	Low frequency
LIB	Lithium-ion battery
LMO	Lithium–manganese-oxide battery
MF	Medium frequency
MR	Mid relaxation time
NMC	Lithium–nickel–manganese–cobalt oxide battery
OC	Operating condition
OCP	Open circuit potential
OCV	Open circuit voltage
OFAT	One factor at a time
PDE	Partial–differential equation
PSO	Particle swarm optimization
R	Relaxation of the developed diagnostic protocol
RMSE	Root mean square error
SD	Standard deviation
SEI	Solid electrolyte interphase
SoC	State of charge
SoH	State of health
SR	Slow relaxation time

List of Symbols

Symbol Latin	Unit of Measure	Description	Symbol Greek	Unit of Measure	Description
a	$[1/m]$	Specific active area	α	$[-]$	Transfer coefficient
A_{el}	$[m^2]$	Electrode area	ε	$[-]$	Material fraction
c	$[mol/m^3]$	Lithium concentration	η	$[V]$	Overpotential
C	$[J/K]$	Heat capacity	κ	$[S/m]$	Ionic conductivity
C_{dl}	$[F/m^2]$	Double layer capacitance	ρ	$[kg/m^3]$	Density
D	$[m^2 \cdot s]$	Lithium diffusion coefficient	φ	$[V]$	Electric potential
EA_k	$[J/mol]$	Rate constant activation energy	**Subscript**		
EA_D	$[J/mol]$	Solid diffusion activation energy	0		Reference
E_{ocp}	$[V]$	Electrode open circuit potential	a		Anodic
F	$[A \cdot s/mol]$	Faraday constant	am		Active material
FCE	$[-]$	Ionic conductivity factor	ax		Axial
h_{conv}	$[W/(m^2 \cdot K)]$	Heat transfer coefficient	c		Cathodic
H	$[m]$	Battery height	e		Electrolyte
i	$[A/m^2]$	Current density	i		Inactive material
i_0	$[A/m^2]$	Exchange current density	max		Maximum
I	$[A]$	Current	min		Minimum
j	$[mol/(m^2 \cdot s)]$	Lithium molar flux	mn		Mandrel
k	$[m/s]$	Rate constant	n		Negative
k_T	$[W/(m \cdot K)]$	Thermal conductivity	nom		Nominal
L	$[m]$	Cell component length	p		Positive
q	$[W \cdot m^{-3}]$	Volumetric heat	r		Reaction
Q	$[mAh]$	Capacity	rad		Radial
r_b	$[m]$	Battery radius	s		Solid
r_p	$[m]$	Particle radius	sc		Steel can
R	$[J \cdot mol^{-1} \cdot K^{-1}]$	Universal gas constant	sep		Separator
R_{ext}	$[\Omega \cdot m^2]$	External resistance	**Superscript**		
R_{film}	$[\Omega \cdot m^2]$	Film resistance	eff		Effective
soc	$[-]$	Electrode state of charge	$"$		Absolute
SOC	$[-]$	Battery state of charge	**Coordinate**		
t_0^+	$[-]$	Lithium transference number	x		Linear coordinate
T	$[K]$	Temperature			Radial coordinate
ΔV	$[V]$	Cell voltage	t		Time
Z	$[\Omega \cdot m^2]$	Impedance	z		Axial coordinate

References

1. Zubi, G.; Dufo-López, R.; Carvalho, M.; Pasaoglu, G. The Lithium-Ion Battery: State of the Art and Future Perspectives. *Renew. Sustain. Energy Rev.* **2018**, *89*, 292–308. [CrossRef]
2. Stampatori, D.; Raimondi, P.P.; Noussan, M. Li-Ion Batteries: A Review of a Key Technology for Transport Decarbonization. *Energies* **2020**, *13*, 2638. [CrossRef]
3. Messing, M.; Shoa, T.; Habibi, S. Estimating Battery State of Health Using Electrochemical Impedance Spectroscopy and the Relaxation Effect. *J. Energy Storage* **2021**, *43*, 103210. [CrossRef]
4. Zhang, Y.; Wik, T.; Bergström, J.; Pecht, M.; Zou, C. A Machine Learning-Based Framework for Online Prediction of Battery Ageing Trajectory and Lifetime Using Histogram Data. *J. Power Sources* **2022**, *526*, 231110. [CrossRef]
5. Meddings, N.; Heinrich, M.; Overney, F.; Lee, J.S.; Ruiz, V.; Napolitano, E.; Seitz, S.; Hinds, G.; Raccichini, R.; Gaberšček, M.; et al. Application of Electrochemical Impedance Spectroscopy to Commercial Li-Ion Cells: A Review. *J. Power Sources* **2020**, *480*, 228742. [CrossRef]
6. Beltran, H.; Ayuso, P.; Vicente, N.; Beltrán-Pitarch, B.; García-Cañadas, J.; Pérez, E. Equivalent Circuit Definition and Calendar Aging Analysis of Commercial Li(NixMnyCoz)O2/Graphite Pouch Cells. *J. Energy Storage* **2022**, *52*, 104747. [CrossRef]
7. Zhang, M.; Liu, Y.; Li, D.; Cui, X.; Wang, L.; Li, L.; Wang, K. Electrochemical Impedance Spectroscopy: A New Chapter in the Fast and Accurate Estimation of the State of Health for Lithium-Ion Batteries. *Energies* **2023**, *16*, 1599. [CrossRef]
8. Li, D.; Yang, D.; Li, L.; Wang, L.; Wang, K. Electrochemical Impedance Spectroscopy Based on the State of Health Estimation for Lithium-Ion Batteries. *Energies* **2022**, *15*, 6665. [CrossRef]
9. Fan, M.; Geng, M.; Yang, K.; Zhang, M.; Liu, H. State of Health Estimation of Lithium-Ion Battery Based on Electrochemical Impedance Spectroscopy. *Energies* **2023**, *16*, 3393. [CrossRef]

10. Tran, M.K.; Mathew, M.; Janhunen, S.; Panchal, S.; Raahemifar, K.; Fraser, R.; Fowler, M. A Comprehensive Equivalent Circuit Model for Lithium-Ion Batteries, Incorporating the Effects of State of Health, State of Charge, and Temperature on Model Parameters. *J. Energy Storage* **2021**, *43*, 103252. [CrossRef]
11. Wang, J.; Jia, Y.; Yang, N.; Lu, Y.; Shi, M.; Ren, X.; Lu, D. Precise Equivalent Circuit Model for Li-Ion Battery by Experimental Improvement and Parameter Optimization. *J. Energy Storage* **2022**, *52*, 104980. [CrossRef]
12. Iurilli, P.; Brivio, C.; Wood, V. On the Use of Electrochemical Impedance Spectroscopy to Characterize and Model the Aging Phenomena of Lithium-Ion Batteries: A Critical Review. *J. Power Sources* **2021**, *505*, 229860. [CrossRef]
13. Krewer, U.; Röder, F.; Harinath, E.; Braatz, R.D.; Bedürftig, B.; Findeisen, R. Review—Dynamic Models of Li-Ion Batteries for Diagnosis and Operation: A Review and Perspective. *J. Electrochem. Soc.* **2018**, *165*, A3656–A3673. [CrossRef]
14. Xu, L.; Lin, X.; Xie, Y.; Hu, X. Enabling High-Fidelity Electrochemical P2D Modeling of Lithium-Ion Batteries via Fast and Non-Destructive Parameter Identification. *Energy Storage Mater* **2022**, *45*, 952–968. [CrossRef]
15. Rabissi, C.; Innocenti, A.; Sordi, G.; Casalegno, A. A Comprehensive Physical-Based Sensitivity Analysis of the Electrochemical Impedance Response of Lithium-Ion Batteries. *Energy Technol.* **2021**, *9*, 2000986. [CrossRef]
16. Rabissi, C.; Sordi, G.; Innocenti, A.; Casalegno, A. Fast and Reliable Calibration of Thermal-Physical Model of Lithium-Ion Battery: A Sensitivity-Based Method. *J. Energy Storage* **2023**, *59*, 106435. [CrossRef]
17. Laue, V.; Röder, F.; Krewer, U. Practical Identifiability of Electrochemical P2D Models for Lithium-Ion Batteries. *J. Appl. Electrochem.* **2021**, *51*, 1253–1265. [CrossRef]
18. Park, M.; Zhang, X.; Chung, M.; Less, G.B.; Sastry, A.M. A Review of Conduction Phenomena in Li-Ion Batteries. *J. Power Sources* **2010**, *195*, 7904–7929. [CrossRef]
19. Valøen, L.O.; Reimers, J.N. Transport Properties of LiPF$_6$-Based Li-Ion Battery Electrolytes. *J. Electrochem. Soc.* **2005**, *152*, A882. [CrossRef]
20. Edouard, C.; Petit, M.; Forgez, C.; Bernard, J.; Revel, R. Parameter Sensitivity Analysis of a Simplified Electrochemical and Thermal Model for Li-Ion Batteries Aging. *J. Power Sources* **2016**, *325*, 482–494. [CrossRef]
21. Zhang, L.; Lyu, C.; Hinds, G.; Wang, L.; Luo, W.; Zheng, J.; Ma, K. Parameter Sensitivity Analysis of Cylindrical LiFePO 4 Battery Performance Using Multi-Physics Modeling. *J. Electrochem. Soc.* **2014**, *161*, A762–A776. [CrossRef]
22. Schmalstieg, J.; Rahe, C.; Ecker, M.; Sauer, D.U. Full Cell Parameterization of a High-Power Lithium-Ion Battery for a Physico-Chemical Model: Part I. Physical and Electrochemical Parameters. *J. Electrochem. Soc.* **2018**, *165*, A3799–A3810. [CrossRef]
23. Ong, J.; Newman, J. Double-Layer Capacitance in a Dual Lithium-Ion Insertion Cell. *J. Electrochem. Soc.* **1999**, *146*, 4360–4365. [CrossRef]
24. Flamme, B.; Rodriguez Garcia, G.; Weil, M.; Haddad, M.; Phansavath, P.; Ratovelomanana-Vidal, V.; Chagnes, A. Guidelines to Design Organic Electrolytes for Lithium-Ion Batteries: Environmental Impact, Physicochemical and Electrochemical Properties. *Green Chem.* **2017**, *19*, 1828–1849. [CrossRef]
25. Carlier, D.; Ménétrier, M.; Delmas, C. 7Li MAS NMR Study of Electrochemically Deintercalated Li$_x$Ni$_{0.30}$Co$_{0.70}$O$_2$ Phases: Evidence of Electronic and Ionic Mobility, and Redox Processes. *J. Mater Chem* **2001**, *11*, 594–603. [CrossRef]
26. Marzec, J.; Przewoźnik, J.P.; Molenda, J.; Simon, D.R.; Kelder, E.M.; Schoonman, J. Conduction Mechanism in Operating a LiMn$_2$O$_4$ Cathode. *Solid State Ion.* **2002**, *146*, 225–237. [CrossRef]
27. Funabiki, A.; Inaba, M.; Ogumi, Z.; Yuasa, S.-I.; Otsuji, J.; Tasaka, A. Impedance Study on the Electrochemical Lithium into Natural Graphite Powder. *J. Electrochem. Soc.* **1998**, *145*, 172. [CrossRef]
28. *IEC 62660-1:2018*; Secondary Lithium-Ion Cells for the Propulsion of Electric Road Vehicles-Part 1: Performance Testing. International Electrotechnical Commission: Geneva, Switzerland, 2018.
29. Park, S.; Kato, D.; Gima, Z.; Klein, R.; Moura, S. Optimal Experimental Design for Parameterization of an Electrochemical Lithium-Ion Battery Model. *J. Electrochem. Soc.* **2018**, *165*, A1309–A1323. [CrossRef]
30. Li, J.; Zou, L.; Tian, F.; Dong, X.; Zou, Z.; Yang, H. Parameter Identification of Lithium-Ion Batteries Model to Predict Discharge Behaviors Using Heuristic Algorithm. *J. Electrochem. Soc.* **2016**, *163*, A1646–A1652. [CrossRef]
31. Yang, X.; Chen, L.; Xu, X.; Wang, W.; Xu, Q.; Lin, Y.; Zhou, Z. Parameter Identification of Electrochemical Model for Vehicular Lithium-Ion Battery Based on Particle Swarm Optimization. *Energies* **2017**, *10*, 1811. [CrossRef]